Int. J. Heat Mass Transfer. Vol. 35, No. 11, pp. 2855–2863, 1992
Printed in Great Britain

0017–9310/92 $5.00 + 0.00

Natural convection–radiation cooling of a vented channel

A. MOUTSOGLOU, J. H. RHEE and J. K. WON
Mechanical Engineering Department, South Dakota State University, Brookings, SD 57007, U.S.A.

(*Received* 8 *June* 1990 *and in final form* 15 *January* 1992)

Abstract—The effects of vent opening size, vent axial location, and number of vents on the combined natural convection–radiation cooling of a one-sided uniformly heated vertical channel in air are numerically investigated. For vented channels the heated wall temperature is shown to increase above the corresponding unvented channel temperatures throughout the region upstream of the farthest from the bottom vent location. For a single low positioned vent, the vented wall temperatures are lower than the corresponding unvented channel temperatures for only a portion of the wall downstream of the vent location. For a continuously heated channel, in general, vents are found to deteriorate the overall cooling process.

INTRODUCTION

NATURAL convection in vertical channels formed by parallel plates has attracted a lot of attention primarily because of the current interest in cooling of electronic equipment. Although many forced or free convection cooling augmentation designs that employ fins are currently in use, often the cooling is influenced by the presence of slits. In natural convection cooling these openings, which may or may not have been purposely designed for cooling augmentation, serve as ports for intake and/or exhaust of ambient air.

Despite its widespread occurrence, a literature survey on heat transfer in vented environments revealed a single prior study on this subject. Azevedo and Sparrow [1] conducted a numerical and experimental study in investigating the natural convection heat transfer and fluid flow characteristics of a one-sided heated channel vented through a single aperture at the unheated wall.

It was found that the average Nusselt numbers for the channel were insensitive to both vent opening size and axial location of the vent. It was revealed that although the presence of the vent opening causes a decrease in the mass flow rate drawn from the bottom of the channel, the total mass flow rate drawn into the channel is only slightly affected.

The local Nusselt number distributions along the heated wall exhibited sharp peaks at the corresponding vent locations. Upstream of the vent location, local Nusselt numbers were found to be lower than those for the unvented channel due to lesser mass flow rate passing through that portion of the channel. It was also experimentally observed that for certain operating conditions, a portion of the fluid entering the vent flowed initially downward along the unheated wall before turning and flowing upward while forming a V-shaped recirculating zone.

In their study, Azevedo and Sparrow [1] considered the heated wall surface to be isothermal. Their results were limited to channels with a single vent with no radiative effects. The present computational study adopts a uniform surface heat flux condition on the heated wall, which better simulates the dissipative heat generation of electronic equipment. Lateral pressure variations in the channel are accounted for in the present study by solving the transverse momentum equation that was otherwise neglected in ref. [1]. Radiative heat transfer among the surfaces is accounted for via an interacting combined convection–surface radiation model. Furthermore, channels with more than one vent are also investigated in the current study.

ANALYSIS

The present study focuses on interacting free convection–surface radiation flow of air, in a one-sided heated vertical channel, in the presence of vent openings at the unheated wall. A schematic view of the flow configuration and coordinate system for a single vent channel is presented in Fig. 1. The channel consists of two vertical infinitely wide parallel plates of finite length L and distance H apart, and has vent openings at the unheated wall. A uniform heat flux q_w is prescribed on the heated surface, and the ambient quiescent air surrounding the channel is assumed to be at a uniform temperature of T_∞. The dimensionless parabolized form of the governing equations for steady, two-dimensional laminar free convection flow of a constant property Boussinesq fluid in a vertical channel can be written as

$$\frac{\partial U}{\partial X}+\frac{\partial V}{\partial Y}=0 \tag{1}$$

$$U\frac{\partial U}{\partial X}+V\frac{\partial U}{\partial Y}=-\frac{\mathrm{d}\bar{P}}{\mathrm{d}X}+\frac{\partial^2 U}{\partial Y^2}+\theta-\theta_\infty \tag{2}$$

NOMENCLATURE

g gravitational accceleration [m s^{-2}]
Gr_H^* modified Grashof number, $g\beta q_w H^4/\nu^2 k$
H channel gap [m]
k thermal conductivity [W m^{-1} K^{-1}]
L channel height [m]
$\dot{m}_{nv}$ mass flow rate of the unvented channel [kg s^{-1}]
$\dot{m}_B$ mass flow rate entering through the bottom of the channel [kg s^{-1}]
$\dot{m}_T$ total mass flow rate leaving the top of the channel [kg s^{-1}]
$\dot{m}_v$ mass flow rate entering through the vent opening [kg s^{-1}]
$\bar{p}$ mean pressure [Pa]
$\hat{p}$ perturbation pressure [Pa]
p_∞ ambient hydrostatic pressure outside of the channel [Pa]
P dimensionless pressure
Pr Prandtl number
q_w uniform heat flux of the heated wall [W m^{-2}]
t vent opening size [m]
T temperature [K]
T_b bulk temperature, equation (22) [K]
T_w heated wall temperature [K]
T_∞ ambient temperature [K]
u, v axial and transverse velocity components [m s^{-1}]
U, V dimensionless axial and transverse velocity components
$\bar{U}$ dimensionless local average velocity, equation (23)
U_B dimensionless uniform inlet velocity at the bottom of the channel
x, y axial and transverse coordinates [m]
X, Y dimensionless axial and transverse coordinates
x_u, x_d axial distance to upstream and downstream edges of vent [m]
X_u, X_d dimensionless axial distance to upstream and downstream edges of vent, equation (12)
x_v axial distance to center of vent [m]
X_v dimensionless axial distance to center of vent, $x_v/H\,Gr_H^*$.

Greek symbols
α thermal diffusivity [m^2 s^{-1}]
β coefficient of thermal expansion [K^{-1}]
ε surface emissivity
θ dimensionless temperature, $kT/q_w H$
θ_∞ dimensionless inlet temperature, $kT_\infty/q_w H$
ν kinematic viscosity [m^2 s^{-1}]
ρ density [kg m^{-3}]
ψ stream function, $u = \partial\psi/\partial y$ [m^2 s^{-1}]
Ψ dimensionless stream function, $\psi/\nu\,Gr_H^*$, equation (21).

$$U\frac{\partial V}{\partial X}+V\frac{\partial V}{\partial Y}=-\frac{\partial \hat{P}}{\partial Y}+\frac{\partial^2 V}{\partial Y^2} \tag{3}$$

$$U\frac{\partial \theta}{\partial X}+V\frac{\partial \theta}{\partial Y}=\frac{1}{Pr}\frac{\partial^2 \theta}{\partial Y^2}. \tag{4}$$

The dimensionless parameters appearing in equations (1)–(4) are defined as

$$X=\frac{x}{H\,Gr_H^*},\quad Y=\frac{y}{H},\quad U=\frac{uH}{\nu\,Gr_H^*}$$

$$V=\frac{vH}{\nu},\quad \bar{P}=\frac{(\bar{p}-p_\infty)H^2}{\rho\nu^2\,Gr_H^*},\quad \hat{P}=\frac{\hat{p}H^2}{\rho\nu^2}$$

$$\theta=\frac{kT}{q_w H},\quad \theta_\infty=\frac{kT_\infty}{q_w H}, \tag{5}$$

where Gr_H^* is the modified Grashof number based on the constant heated wall flux q_w:

$$Gr_H^*=\frac{g\beta q_w H^4}{\nu^2 k}. \tag{6}$$

The flow boundary conditions for the channel can be written as

$$U=U_B,\quad V=0,\quad \bar{P}=-U_B^2/2\quad \text{at}\quad X=0 \tag{7}$$

$$U=V=0\quad \text{at}\quad Y=0 \tag{8}$$

$U=V=0$ at $Y=1$ and

$$\begin{cases} 0<X\leqslant X_{u_1} \\ X_{d_{k-1}}<X\leqslant X_{u_k} \quad \text{for} \quad k=2,3,\ldots,K \\ X_{d_K}<X\leqslant L/H\,Gr_H^* \end{cases} \tag{9}$$

$$V=(-2\bar{P}\,Gr_H^{*2})^{1/2},\quad U=0\quad \text{at}\quad Y=1$$
$$\text{and}\quad X_{u_k}<X\leqslant X_{d_k}\quad \text{for}\quad k=1,2,\ldots,K \tag{10}$$

$$\bar{P}=0\quad \text{at}\quad X=L/H\,Gr_H^*. \tag{11}$$

In the equations above, U_B is the unknown uniform inlet velocity at the bottom of the channel, K is the number of vents, and X_{u_k} and X_{d_k} denote the dimensionless upstream and downstream edges of the kth vent given from

$$X_{u_k}=X_{v_k}-\frac{t_k/H}{2\,Gr_H^*},\quad X_{d_k}=X_{v_k}+\frac{t_k/H}{2\,Gr_H^*} \tag{12}$$

where $X_{v_k}=x_{v_k}/H\,Gr_H^*$ is the dimensionless axial distance to the center of the vent, and t is the length of the vent opening.

The velocity boundary conditions at the vent open-

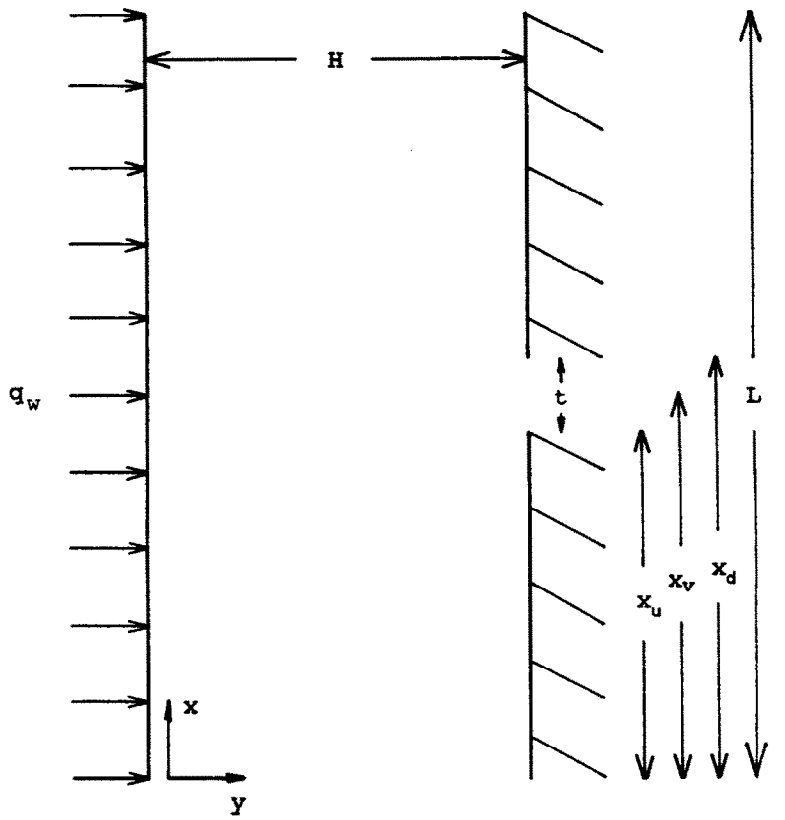

FIG. 1. Schematic view and coordinate system.

ing (equation (10)), consistent with ref. [1], were estimated by assuming the fluid to enter the channel horizontally and by employing Bernoulli's equation. The mean pressure at the inlet of the channel was also estimated from Bernoulli's equation.

The thermal boundary conditions are specified as

$$\theta = \theta_\infty \quad \text{at} \quad X = 0 \tag{13}$$

$$1 = -\left.\frac{\partial\theta_i}{\partial Y}\right|_{Y=0} + \varepsilon_i R\theta_i^4|_{Y=0} - \varepsilon_i \sum_{m=1}^{M} F_{i-m}\left[\frac{(1-\varepsilon_m)}{\varepsilon_m}\left.\frac{\partial\theta_m}{\partial Y}\right|_{Y=1} + R\theta_m^4|_{Y=1}\right] - \varepsilon_i F_{i-\text{top}} R\theta_\infty^4 - \varepsilon_i F_{i-\text{bot}} R\theta_\infty^4 - \varepsilon_i R\theta_\infty^4 \sum_{k=1}^{K} F_{i-\text{vent}_k}$$

$$\text{at} \quad Y = 0 \quad \text{for} \quad i = 1,2,\ldots,N \tag{14}$$

$$0 = \left.\frac{\partial\theta_j}{\partial Y}\right|_{Y=1} + \varepsilon_j R\theta_j^4|_{Y=1} - \varepsilon_j \sum_{n=1}^{N} F_{j-n} \times\left[\frac{(1-\varepsilon_n)}{\varepsilon_n}\left(-\left.\frac{\partial\theta_n}{\partial Y}\right|_{Y=0} - 1\right) + R\theta_n^4|_{Y=0}\right] - \varepsilon_j F_{j-\text{top}} R\theta_\infty^4 - \varepsilon_j F_{j-\text{bot}} R\theta_\infty^4$$

$$\text{for} \quad j = 1,2,\ldots,M \tag{15}$$

at $Y = 1$ and

$$\begin{cases} 0 < X \leqslant X_{u_1} \\ X_{d_{k-1}} < X \leqslant X_{u_k} \quad \text{for} \quad k = 2,3,\ldots,K \\ X_{d_K} < X \leqslant L/H\, Gr_H^* \end{cases}$$

$$\theta = \theta_\infty \quad \text{at} \quad Y = 1 \quad \text{and} \quad X_{u_k} < X \leqslant X_{d_k} \quad \text{for} \quad k = 1,2,\ldots,K \tag{16}$$

where N is the number of elemental surfaces on the heated wall and M is the number of elemental surfaces on the unheated wall. The radiation number R is defined as

$$R = \frac{\sigma q_{\text{ref}}^3 H^4}{k^4}. \tag{17}$$

All surfaces were assumed to be gray and opaque, and the temperature of the surroundings was taken to be that of the quiescent ambient air T_∞. The shape factors appearing in equations (14) and (15) were evaluated systematically via a combination of Hottel's rule and the decomposition rule.

COMPUTATIONAL PROCEDURE

The dimensionless system of governing conservation equations (1)–(4) along with the corresponding boundary conditions (equations (7)–(11)

and (13)–(16)) were solved by utilizing the Patankar–Spalding [2] finite difference scheme tailored for parabolic equations, while adopting the Simpler algorithm of Patankar [3] for treating the convection–diffusion terms.

A Gauss–Seidel iterative scheme was employed for handling the radiative terms in the thermal boundary conditions. Consequently the procedure required the linearization of just the second term on the right-hand side of equations (14) and (15). This was done using a Taylor series type of linearization:

$$\theta^4 \simeq \theta^{*4} + 4\theta^{*3}(\theta - \theta^*) \tag{18}$$

where θ^* is the current iterative value of the wall temperature. The remaining terms, in equations (14) and (15), that involve temperatures raised to the fourth power were left as they are, and were evaluated from their current iterative values.

Sixty-four grid points were deployed in the transverse direction while 240 streamwise stations were selected. A variable grid size was utilized to account for the rapid axial and transverse variations of the channel velocity and temperature at the beginning of each wall segment. The streamwise grid interspace increased monotonically in the X-direction. The grid interspace in the transverse Y-direction increased symmetrically from either side to the center of the channel.

Numerical tests with 32 transverse and 120 streamwise grid points produced mass flow rates and maximum wall temperatures that differed by less than 0.5% from the corresponding results with the chosen mesh of 64×240.

RESULTS

The computational algorithm was first tested by comparing the present results for water, in the absence of radiation, for an isothermally one-sided heated channel with a single vent, to the numerical data reported by Azevedo and Sparrow [1]. Ratios of mass flow rates entering the channel via the vent, $\dot{m}_v$, to those entering through the bottom principal opening, $\dot{m}_B$, and ratios of total mass flow rate drawn into the channel through the bottom and vent, $\dot{m}_T$, to those drawn through a similar channel with no vent, $\dot{m}_{nv}$, are plotted in Fig. 2. The data pertain to the set-up of Fig. 7 in ref. [1], which corresponds to $Pr = 5$, $L/(H\,Gr_H) = 0.0167$, and $Gr_H = 1852$, where the Grashof number is defined as $Gr_H = g\beta(T_w - T_\infty)H^3/\nu^2$. The present data seem to correlate well with the numerical data of ref. [1] considering that the data are read directly from Fig. 7 of ref. [1].

The slight deviations of the mass flow rates in Fig. 2 may be attributed to the inclusion of the transverse momentum equation in the present study. More importantly, however, the consideration of the transverse momentum equation seems to greatly influence the convergence of the present algorithm. It was found that as the vent was positioned farther from the bottom (increasing x_v/L) the algorithm failed to converge

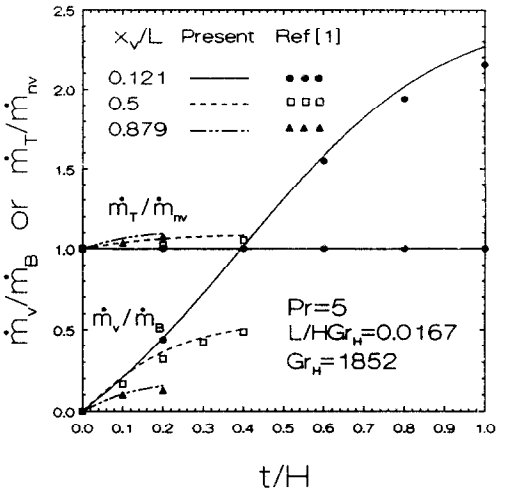

FIG. 2. Mass flow rates of water for a one-sided isothermally heated channel with a single vent, $Pr = 5$.

beyond smaller vent-size openings t/H. Thus, as can be seen from Fig. 2, while no convergence problems were encountered for the lower positioned vent ($x_v/L = 0.121$), the algorithm failed to converge for the middle positioned vent ($x_v/L = 0.5$) when t/H was greater than 0.4, and for the upper positioned vent ($x_v/L = 0.879$) when t/H was greater than 0.2. The failure of convergence is attributed to the near-the-vent downward flow that must develop in these instances, as reported under certain operating conditions in the flow visualization experiments of ref. [1]. This is corroborated by the negative streamwise velocities predicted by the present numerical algorithm near the upstream of the lower edge of the vent, where the solution failed to converge. No negative velocities or failure of convergence, on the other hand, were reported in ref. [1], where the transverse momentum equation was neglected and data were presented for $0 \leqslant t/H \leqslant 1$ for all three vent locations. The present findings suggest that downstream flow is triggered by larger vent-size openings and larger bottom-to-center of vent distances, as well as larger Grashof numbers as hinted in ref. [1] and verified by numerical experimentation in the present study.

Computational data are presented for mean pressure variations, mass flow rates, axial temperature distribution of the heated wall, bulk temperatures, and streamwise and transverse velocity and temperature profiles for air. In the system of equations (1)–(4), (7)–(11), (13)–(16) the governing dimensionless parameters Gr_H^*, Pr, θ_∞, R, L/H, t/H and x_v/L are functions of six physical dimensional variables, in addition to the surface emissivities and thermophysical properties of the fluid. These are the channel length L, channel width H, vent length t, axial distance to the center of the vent x_v, fluid inlet temperature T_∞, and the prescribed uniform heat flux q_w. Numerical results are obtained for the following configuration:

$$L = 140 \text{ mm}, \quad H = 11.568 \text{ mm}, \quad t = 3.470 \text{ mm}$$

$$x_v = 21 \text{ mm and/or } 70 \text{ mm}, \quad T_\infty = 300 \text{ K}$$

$$q_w = 183.208 \text{ W m}^{-2}, \quad \varepsilon = 0.2. \tag{19}$$

The emissivities of the surfaces were taken to be equal to 0.2, which is characteristic of printed circuit boards. The thermophysical properties of air were estimated at the inlet air temperature of $T_\infty = 300$ K. These combinations resulted in the following dimensionless parameters:

$$Gr_H^* = 16\,137, \quad Pr = 0.707, \quad \theta_\infty = 3.723$$

$$R = 0.013, \quad L/H = 12.103, \quad t/H = 0.3$$

$$x_v/L = 0.15 \text{ and/or } 0.5. \tag{20}$$

Streamwise variations of the mean pressure imbalance for single and double vented channels ($x_v/L = 0.15$ and/or 0.5, $t/H = 0.3$), and a corresponding unvented channel are shown in Fig. 3. Significantly smaller magnitudes in mean pressure are experienced for the vented channels as a result of the inside–outside fluid communication through the vents. Consequently, as dictated from Bernoulli's equation at the inlet (equation (7)), the air drawn through the bottom opening of the vented channel is less than the corresponding flow rate for the unvented channel. The sudden increase in the magnitude of the mean pressure imbalance near the location of the vent(s) ($x/L = 0.15$ and/or 0.5) signifies the increase in the total air flow rate in the channel due to mass flowing in through the vent.

Cross-channel distributions for streamwise velocity, transverse velocity and air temperatures are depicted at four axial locations for a single vented channel

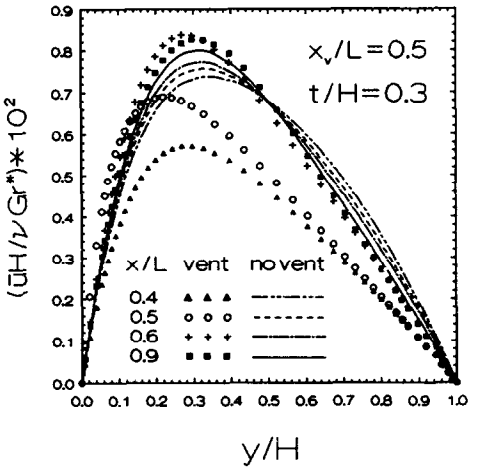

FIG. 4. Streamwise velocity profiles of air for vented and unvented channels; $L = 140$ mm, $H = 11.568$ mm, $T_\infty = 300$ K, $q_w = 183.208$ W m^{-2}, $\varepsilon = 0.2$.

in Figs. 4, 5 and 6, respectively. The data are for a vent centered at mid-channel $x_v/L = 0.5$ with a gap size of $t/H = 0.3$. The first three axial distances pertain to streamwise locations before, at, and after the vent, while the last one corresponds to a location near the top of the channel. Results for an unvented channel are also plotted in the same figures at the corresponding streamwise locations.

As noted from Fig. 4, the streamwise velocities for a vented channel are significantly lower than the corresponding velocities for an unvented channel at locations below the vent. As the area under the curve signifies mass flow rates, less air is drawn from the bottom of the vented channel in accordance with the discussion of Fig. 3. At $x/L = 0.5$, where the center of the vent is located, streamwise velocities throughout

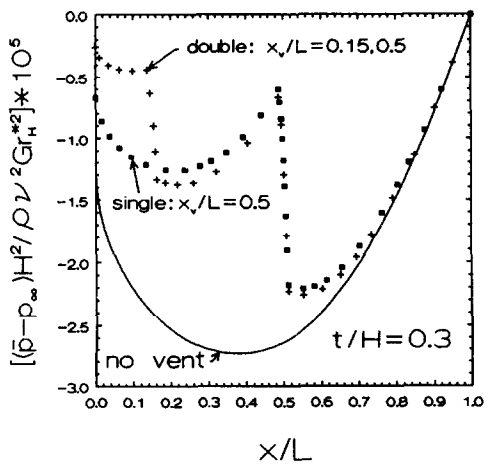

FIG. 3. Mean pressure variation of air for single or double vented and unvented channels; $L = 140$ mm, $H = 11.568$ mm, $T_\infty = 300$ K, $q_w = 183.208$ W m^{-2}, $\varepsilon = 0.2$.

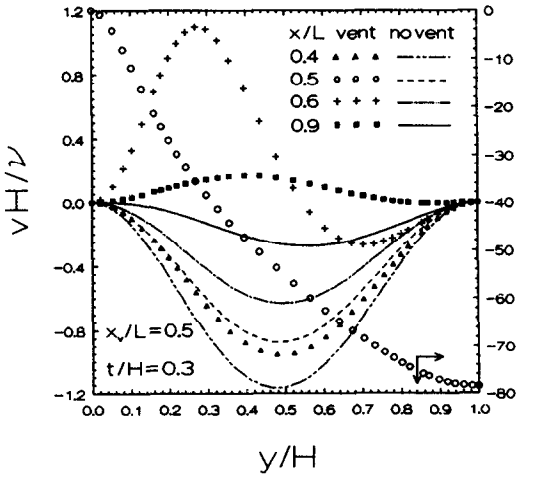

FIG. 5. Transverse velocity profiles of air for vented and unvented channels; $L = 140$ mm, $H = 11.568$ mm, $T_\infty = 300$ K, $q_w = 183.208$ W m^{-2}, $\varepsilon = 0.2$.

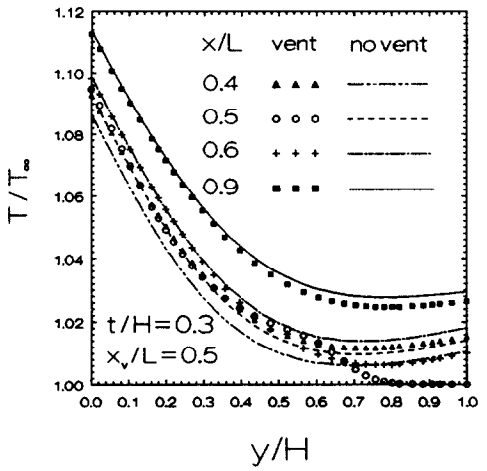

FIG. 6. Cross-channel temperature profiles of air for vented and unvented channels; $L = 140$ mm, $H = 11.568$ mm, $T_\infty = 300$ K, $q_w = 183.208$ W m^{-2}, $\varepsilon = 0.2$.

the channel width increase as fluid is drawn in through the vent. Velocities, particularly near the heated wall, increase significantly due to the fluid entering horizontally from the vent. The largest velocity gradients near the heated wall occur at locations corresponding to the vent. At an axial location above the vent, $x/L = 0.6$, the flow readjusts by spreading over the entire width of the channel and the profile becomes fuller. It is interesting to note that near the exit of the channel, $x/L = 0.9$, the velocity profiles of the vented and unvented channels are quite similar; this is indicative of the closeness of the corresponding total mass flow rates for the two cases.

Transverse velocity profiles at the respective four axial locations are plotted in Fig. 5. The transverse velocity profiles for the unvented channel are nearly symmetric, having small negative values. For a vented channel, at locations upstream of the vent, $x/L = 0.4$, the profiles are of the same general shape having smaller negative values as the upstream flow rate is smaller for the vented channel. At axial locations of the vent, $x/L = 0.5$, the magnitude of the negative transverse velocities increases significantly due to the fluid entering through the vent. The velocities are negative throughout the channel. Downstream of the vent, $x/L = 0.6$, the fluid readjusts by moving away from the two walls. Finally, at $x/L = 0.9$, transverse velocities are nearly zero, indicating fully developed conditions.

The corresponding cross-channel temperature distributions are shown at the same four axial locations in Fig. 6. Upstream of the vent, $x/L = 0.4$, as less fluid is drawn from the bottom of the vented channel, the air is warmer than the air in the unvented channel. At the vent location, $x/L = 0.5$, the cooler ambient fluid entering through the vent lowers the temperature of the air in the channel. The temperature of the air increases with axial distance downstream of the vent, and near the exit of the channel, $x/L = 0.9$, the temperature profiles of the vented and unvented channels become quite similar.

To illustrate the streamlines in a vented channel, a dimensionless stream function $\Psi = \psi/\nu\, Gr_H^*$, determined from

$$\Psi = \int_0^Y U\, dY, \tag{21}$$

is plotted in Fig. 7 for a vent centered at mid-channel, $x_v/L = 0.5$, with a gap size of $t/H = 0.3$. The corresponding isotherms, T/T_∞, are shown in Fig. 8. The contour plots provide a general view of the aforementioned trends discussed in Figs. 4–6.

Transverse velocities near the lower and upper portions of the vent are displayed in Fig. 9 for a channel with a single vent located at a lower ($x_v/L = 0.15$) or middle ($x_v/L = 0.5$) portion of the channel. The vent-size opening in each case is fixed at $t/H = 0.3$. The magnitude of the negative transverse velocities throughout the vent at $y/H = 1$ decreases as the vent location moves farther from the bottom. Regardless of the axial location of the vent, the magnitude of the vent velocities at $y/H = 1$ increases from the bottom edge to the top edge of the vent. Transverse velocity profiles at the bottom edge of the vent exhibit peaks for a short region away from the bottom, and then farther downstream they monotonically decrease to zero at the heated wall.

Dimensionless local bulk temperatures are calculated from

$$\frac{T_b}{T_\infty} = \int_0^1 \frac{U\theta}{\bar{U}\theta_\infty}\, dY \tag{22}$$

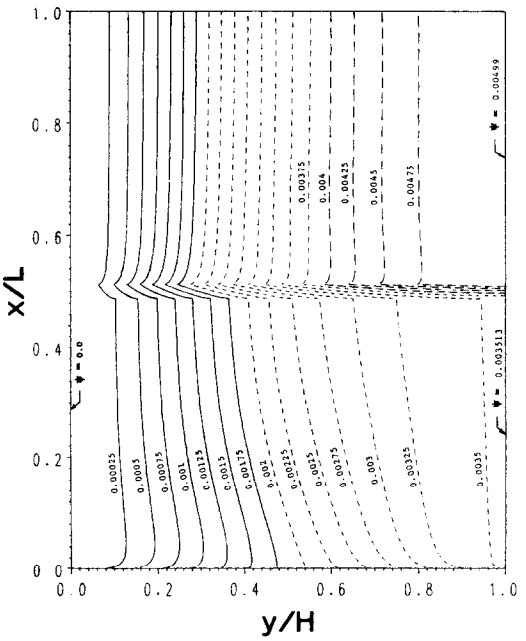

FIG. 7. Streamlines of air for a vented channel; $x_v/L = 0.5$, $t/H = 0.3$, $L = 140$ mm, $H = 11.568$ mm, $T_\infty = 300$ K, $q_w = 183.208$ W m^{-2}, $\varepsilon = 0.2$.

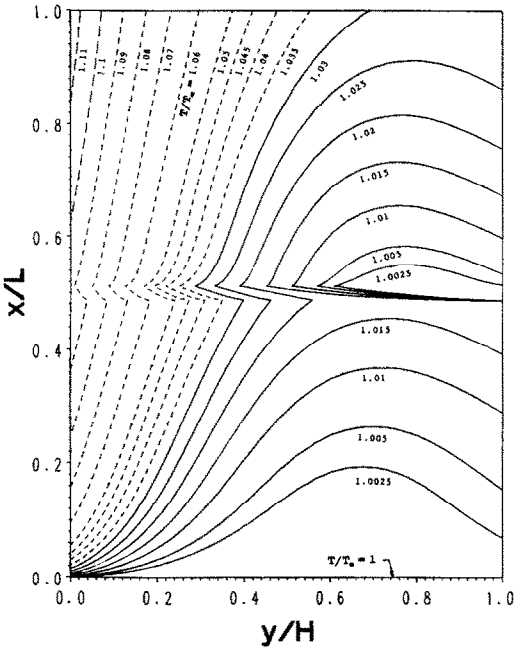

FIG. 8. Isotherms of air for a vented channel; $x_v/L = 0.5$, $t/H = 0.3$, $L = 140$ mm, $H = 11.568$ mm, $T_\infty = 300$ K, $q_w = 183.208$ W m^{-2}, $\varepsilon = 0.2$.

where $\bar{U}$ is the dimensionless local average velocity defined as

$$\bar{U} = \int_0^1 U \, dY. \tag{23}$$

Bulk temperature variations of air for a channel with single and double vents are illustrated in Fig. 10 for $t/H = 0.3$. The bulk temperature, consistent with the uniform heating rate prescribed at the wall, increases linearly in the axial direction with the slope of each line directly proportional to the local mass flow rate. At the vent location, there is a sharp drop-off in the bulk temperature due to the cool air introduced through the vent opening. Overall energy balances written in dimensionless form,

$$\frac{T_{b_L}}{T_\infty} = 1 + \frac{(L/H)}{\bar{U}_T \theta_\infty \, Gr_H^* \, Pr}, \tag{24}$$

were satisfied within 0.5% for all four cases indicated in Fig. 10. In equation (24), T_{b_L} is the bulk temperature of the air at the dimensionless channel exit and $\bar{U}_T$ is the dimensionless average velocity at the top of the channel.

Mass flow rates, in terms of $\dot{m}_v/\dot{m}_B$ and $\dot{m}_T/\dot{m}_{nv}$ ratios, are shown in Fig. 11 for a single vented channel as a function of the vent-size opening. The total mass flow rate drawn into the channel increases only slightly for a fixed vent opening as the vent location moves downstream. On the other hand, the ratio of

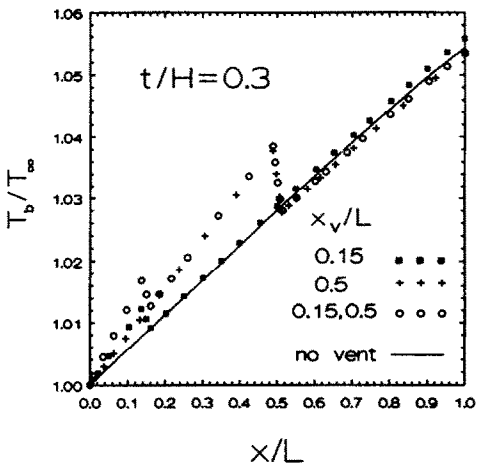

FIG. 10. Bulk temperatures of air for single vented and unvented channels; $L = 140$ mm, $H = 11.568$ mm, $T_\infty = 300$ K, $q_w = 183.208$ W m^{-2}, $\varepsilon = 0.2$.

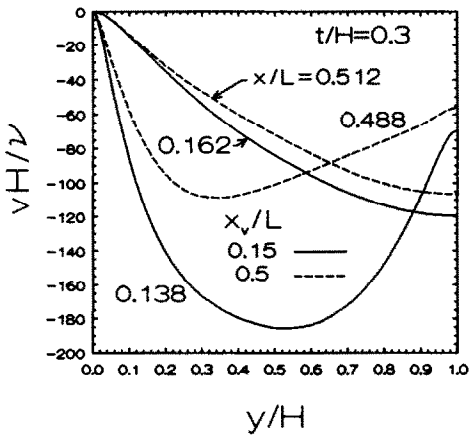

FIG. 9. Transverse velocity profiles of air near the lower and upper edges of single vented channels; $L = 140$ mm, $H = 11.568$ mm, $T_\infty = 300$ K, $q_w = 183.208$ W m^{-2}, $\varepsilon = 0.2$.

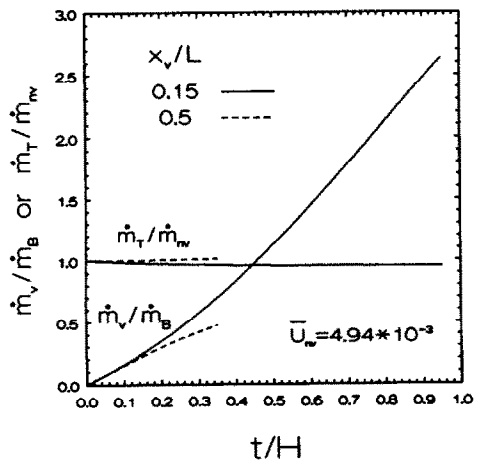

FIG. 11. Mass flow rates of air in single vented channels; $L = 140$ mm, $H = 11.568$ mm, $T_\infty = 300$ K, $q_w = 183.208$ W m^{-2}, $\varepsilon = 0.2$.

Table 1. Mass flow rate ratios for single and double vented channels; $L = 140$ mm, $H = 11.5686$ mm, $t = 3.47$ mm, $T_\infty = 300$ K, $q_w = 183.208$ W m^{-2}, $\varepsilon = 0.2$, $\dot{m}_{nv}$/depth $= 1.47 \times 10^{-3}$ kg s^{-1} m^{-1}

Condition	x_v/L	$\dot{m}_{v_{low}}/\dot{m}_{nv}$	$\dot{m}_{v_{mid}}/\dot{m}_{nv}$	$\dot{m}_B/\dot{m}_{nv}$	$\dot{m}_T/\dot{m}_{nv}$
Single	0.15	0.351		0.615	0.966
Single	0.5		0.299	0.710	1.009
Double	0.15; 0.5	0.242	0.306	0.445	0.994

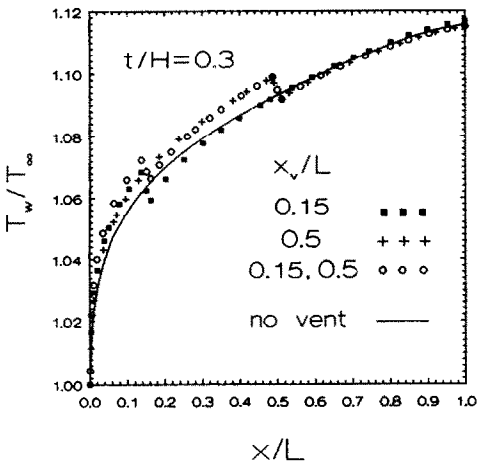

FIG. 12. Heated wall temperatures for single or double vented, and unvented channels; $L = 140$ mm, $H = 11.568$ mm, $T_\infty = 300$ K, $q_w = 183.208$ W m^{-2}, $\varepsilon = 0.2$.

the flow rate through the vent to the flow rate through the bottom of the channel, $\dot{m}_v/\dot{m}_B$, for a given opening of the vent, decreases considerably as the vent is situated farther from the bottom. This is because as the distance from the bottom of the channel to the vent increases, the flow rate entering from the bottom increases while the flow rate entering through the vent decreases. As noted from Fig. 11 for the lower ($x_v/L = 0.15$) and the mid-centered ($x_v/L = 0.5$) vents, the solution fails to converge for vent gap sizes beyond $t/H = 0.95$ and 0.35, respectively, possibly signaling downward flow in these instances. The local dimensionless average velocity $\bar{U}$ may be estimated from the ratios of mass flow rates (Fig. 11) and the knowledge of the corresponding average velocity $\bar{U}_{nv}$ for unvented channels. For the specified conditions of equation (20), the average velocity of the unvented channel is found to be $\bar{U}_{nv} = 4.94 \times 10^{-3}$. Comparative data for mass flow rate ratios are compiled in Table 1 for $t/H = 0.3$.

The axial variation of the heated wall temperature for single and double vented channels is plotted in Fig. 12 for $t/H = 0.3$. The wall temperature variation for the unvented channel is illustrated by a solid line. As noted from the figure, for single vents, the heated wall temperatures considerably exceed the corresponding unvented channel temperatures throughout the region upstream of the vent. Also, as can be seen from the figure, for single vents, the temperature drop of the heated wall across the vent decreases as the location of the vent moves farther from the bottom. This is due to the smaller amount of cool air entering through the vent as the vent location moves upward. For the low position vent ($x_v/L = 0.15$), the wall temperature becomes of the same order as that for the unvented case around $x/L = 0.5$. Farther downstream, the heated wall temperatures exceed the corresponding temperatures for the unvented case. The above trends indicate that, in general, the presence of slits in channels may be more detrimental than beneficial in the cooling of the heated surface.

CONCLUSIONS

The effects of vents in natural convection–radiation cooling of a one-sided heated vertical channel with a prescribed uniform heat flux are numerically investigated. The failure of convergence of the solution algorithm for certain vent configurations hints the presence of downward flow reported in the flow visualization experiments of Azevedo and Sparrow [1]. For a continuously heated surface, as is the case with the present study, in general, the presence of vents is shown to hinder the overall cooling process.

REFERENCES

1. L. F. A. Azevedo and E. M. Sparrow, Natural convection in a vertical channel vented to the ambient through an aperture in the channel wall, *Int. J. Heat Mass Transfer* **29**, 819–830 (1986).
2. S. V. Patankar and D. B. Spalding, A calculation procedure for heat, mass, and momentum transfer in three-dimensional parabolic flows, *Int. J. Heat Mass Transfer* **15**, 1787–1806 (1972).
3. S. V. Patankar, *Numerical Heat Transfer and Fluid Flow*. Hemisphere, Washington, DC (1980).
4. G. D. Raithby and G. E. Schneider, Numerical solution of problems in incompressible fluid flow: treatment of velocity–pressure coupling, *Numer. Heat Transfer* **2**, 417–440 (1979).

REFROIDISSEMENT PAR CONVECTION NATURELLE ET RAYONNEMENT D'UN CANAL AVEC EVENT

Résumé—On étudie numériquement les effets de la taille d'une ouverture, la localisation axiale de cet évent et le nombre d'évents sur le refroidissement, par convection naturelle d'air combinée au rayonnement, d'un canal vertical chauffé uniformément sur un seul côté. Pour de tels canaux la température de la paroi chaude augmente au dessus des températures du canal correspondant sans évent partout dans la région au dessus de l'évent le plus éloigné de la base. Pour un évent unique positionné en bas, les températures de la paroi avec évent sont inférieures à celles d'un canal correspondant sans évent pour seulement une portion de la paroi au dessous de la localisation de l'évent. Pour un canal continûment chauffé, en général, des évents détériorent le mécanisme global du refroidissement.

KÜHLUNG EINES BELÜFTETEN KANALS DURCH NATÜRLICHE KONVEKTION UND STRAHLUNG

Zusammenfassung—In der vorliegenden Arbeit werden die Einflüsse von Größe, axialer Position und Anzahl der Lüftungsöffnungen auf die kombinierte Kühlwirkung durch natürliche Konvektion und Strahlung in einem einseitig gleichförmig beheizten, senkrechten luftgefüllten Kanal numerisch untersucht. In einem belüfteten Kanal zeigt sich, daß die Temperatur der beheizten Wand größer ist als die entsprechende Temperatur in einem unbelüfteten Kanal; dies gilt für das gesamte Gebiet stromaufwärts von demjenigen Ort, der am weitesten von einer unten gelegenen Lüftungsöffnung entfernt ist. Für eine einzelne unten angebrachte Lüftungsöffnung sind die Wandtemperaturen mit Belüftung kleiner als diejenigen ohne Belüftung, jedoch nur für einen Teil der Wand stromabwärts von der Lüftungsöffnung. In einem kontinuierlich beheizten Kanal reduzieren im allgemeinen Lüftungsöffnungen die Kühlwirkung insgesamt.

ОХЛАЖДЕНИЕ ВЕНТИЛИРУЕМОГО КАНАЛА ЕСТЕСТВЕННОЙ КОНВЕКЦИЕЙ И ИЗЛУЧЕНИЕМ

Аннотация—Численно исследуется влияние размера, осевого расположения относительно оси и количества отверстий на взаимосвязанное охлаждение естественной конвекцией и излучением вертикального канала, равномерно нагреваемого с одной стороны и находящегося в воздушной среде. Показано, что температура нагретых стенок вентилируемых каналов превышает соответствующие температуры невентилируемых каналов на всем участке вверх по течению. В случае единичного низко расположенного отверстия температцры стенок с отверстиями ниже соответствующих температур для невентилируемых каналов только на участке вниз по потоку от отверстия. Для каиала, нагреваемого постоянным тепловым потоком, найдено, что наличие отверстий обычно приводит к ухудшению общего процесса охлаждения.